V European Conference on Computational Fluid Dynamics
ECCOMAS CFD 2010
J. C. F. Pereira and A. Sequeira (Eds)
Lisbon, Portugal,14-17 June 2010

EQUIVALENCE CONDITIONS FOR FINITE VOLUME / ELEMENT DISCRETIZATIONS IN CYLINDRICAL COORDINATES

Dante De Santis, Gianluca Geraci and Alberto Guardone

[†]Dipartimento di Ingegneria Aerospaziale, Politecnico di Milano Via La Masa, 34, 20156 Milano, Italy
e-mail: alberto.guardone@polimi.it

Key words: Compressible flows, Shock waves, Explosion/Implosion problem, Cylindrical coordinates, Finite Element/Volume Methods

Abstract. *A novel numerical technique for the solution of the compressible flow equations over unstructured grids in a cylindrical reference is presented. The proposed approach is based on a mixed finite volume / finite element method. Equivalence conditions relating the finite volume and the finite element metrics in cylindrical coordinates are derived. Numerical simulations of the explosion and implosion problems for inviscid compressible flows are carried out to evaluate the correctness of the numerical scheme. For the implosion problem, numerical simulations include also the effect of the presence of cylindrical obstacles in the flow field, which have been recently proposed as a mean to modify the shape of a cylindrical converging shock to increase the shock front stability in experimental studies on the sonoluminescence effect. Spherical shock waves are also considered and the modification to the shock geometry due to the presence of a spherical obstacle is evaluated numerically and compared to its cylindrical counterpart.*

1 INTRODUCTION

In a cylindrical reference, diverse gasdynamics problems exhibit relevant symmetries. These are, e.g., nozzle flows, detonations, astrophysical flows, Inertial Confinement Fusion (ICF) applications, sonoluminescence phenomena and nuclear explosions.[1] To compute the numerical solution of the compressible flow equations for these kind of flows, an interesting possibility is provided by the use of a mixed finite volume (FV) / finite element (FE) approach,[2] which has been already successfully applied to the multidimensional Cartesian case[3,4] and the cylindrical case with axial symmetry.[6] For example, in viscous flows, it is possible to use the FV and the FE to compute the advection and dissipation terms, respectively, within the same algorithm. Such a possibility is expected to be of use in the study of the effect of viscosity on e.g. the formation of stable shock fronts in cylindrically and spherically symmetric problems and on the determination of the onset and dynamics of Richtmyer-Meshkov instabilities in cylindrical and spherical implosions.[5]

The combined use of these two different techniques is made possible by the introduction of suitable equivalence conditions that relate the FV metrics, i.e. cell volumes and integrated normals, to the FE integrals. Equivalence conditions relating FV and FE schemes have been derived for Cartesian coordinates in two and three spatial dimensions[3,4] and for cylindrical coordinates in axially symmetric two-dimensional problems.[6] In both cited references, equivalent conditions are obtained by neglecting higher order FE contributions. In the present paper, equivalence conditions for the cylindrical coordinates (Z, R, θ), with Z, R and θ axial, radial and azimuthal coordinate, respectively, are derived for the first time without introducing any approximation into the FE discrete expression of the divergence operator. In particular, three independent equivalent conditions are introduced to link all FV and FE metric quantities defined over the computational grid.

The present paper is structured as follows. In section 2, the FE and FV schemes are briefly described for a scalar conservation law. Equivalence conditions are demonstrated in this case. The extension to the system of Euler equations for compressible flow is also sketched. In section 3, numerical simulations are presented for the explosion and implosion problem in the cylindrical coordinates, including both the axisymmetric (Z-R plane) and the polar (R-θ) case, and are compared to one-dimensional simulations. The effect of introducing cylindrical obstacles in the flow field is also investigated numerically and the modification to the geometry of the cylindrical converging shock wave is studied. The case of spherical shock waves is also considered and the modification to the shock geometry due to the presence of a spherical obstacle is evaluated. In section 4 final remarks and comments are given.

2 FINITE VOLUME/ELEMENT METHOD IN CYLINDRICAL COORDINATES

In the present section, the finite element and finite volume discrete equations for a scalar conservation law in a three-dimensional cylindrical reference are given. The model

equation reads

$$\frac{\partial u}{\partial t} + \frac{\partial f_Z}{\partial Z} + \frac{1}{R}\frac{\partial}{\partial R}(R f_R) + \frac{1}{R}\frac{\partial f_\theta}{\partial \theta} = 0, \tag{1}$$

where t is the time, Z, R and θ are the axial, radial and azimuthal coordinates, respectively, $u = u(Z, R, \theta, t)$ is the scalar unknown and $\boldsymbol{f}^{\varnothing}(u) = (f_Z, f_R, f_\theta)$ is the so-called flux function. A more compact form of the above equation is obtained by introducing the divergence operator in three-dimensional cylindrical coordinates $\boldsymbol{\nabla}^{\varnothing}\boldsymbol{\cdot}\,(\cdot)$ as follows

$$\frac{\partial (u)}{\partial t} + \boldsymbol{\nabla}^{\varnothing}\boldsymbol{\cdot}\,\boldsymbol{f}^{\varnothing}(u) = 0. \tag{2}$$

Equivalence conditions relating the FV and the FE approaches are then derived in the three-dimensional case. Finally, the numerical scheme is applied to the compressible Euler equations and time discretization is discussed.

2.1 Node-pair finite element discretization

The scalar conservation law (2) is now written in a weak form by multiplying it by the radial coordinate R and by a suitable Lagrangian test function $\phi_i \in V_h \subset H^1(\Omega)$. Integrating over the support Ω_i of ϕ_i gives

$$\int_{\Omega_i} R\phi_i \frac{\partial u}{\partial t}\, d\Omega_i + \int_{\Omega_i} R\phi_i \boldsymbol{\nabla}^{\varnothing}\boldsymbol{\cdot}\,\boldsymbol{f}^{\varnothing}(u)\, d\Omega_i = 0, \quad \forall i \in \mathcal{N}, \tag{3}$$

where $\mathcal{N}$ is the set of all nodes of the triangulation. Note that by multiplying by R, the numerical singularity of the cylindrical reference system is formally removed.[6] In the following, to simplify the notation, the infinitesimal volume $d\Omega = RdRd\theta dZ$ is not indicated in the integrals. Integrating by parts immediately gives

$$\int_{\Omega_i} R\phi_i \frac{\partial u}{\partial t} = \int_{\Omega_i} R\boldsymbol{f}^{\varnothing}\boldsymbol{\cdot}\,\boldsymbol{\nabla}^{\varnothing}\phi_i + \int_{\Omega_i} \phi_i \boldsymbol{f}^{\varnothing}\boldsymbol{\cdot}\,\boldsymbol{\nabla}^{\varnothing} R - \int_{\partial\Omega_i^{\partial}} R\phi_i \boldsymbol{f}^{\varnothing}\boldsymbol{\cdot}\,\boldsymbol{n}_i^{\varnothing} \tag{4}$$

where $\partial\Omega_i^{\partial} = \partial\Omega_i \cap \partial\Omega$, with $\partial\Omega_i$ and $\partial\Omega$ are the boundary of Ω_i and of the computational domain Ω, respectively, and where $\boldsymbol{n}_i^{\varnothing} = n_Z\hat{\boldsymbol{Z}} + n_R\hat{\boldsymbol{R}} + n_\theta\hat{\boldsymbol{\theta}}$ is the outward normal versor to Ω_i. The scalar unknown is now interpolated as

$$u(Z, R, \theta, t) \simeq u_h(Z, R, \theta, t) = \sum_{k\in\mathcal{N}} u_k(t)\phi_k(Z, R, \theta),$$

to obtain the Bubnov-Galerkin approximation of (2), namely,

$$\sum_{k\in\mathcal{N}_i} M_{ik}^{\varnothing}\frac{\mathrm{d}u_k}{\mathrm{d}t} = \int_{\Omega_i} R\boldsymbol{f}^{\varnothing}(u_h)\boldsymbol{\cdot}\,\boldsymbol{\nabla}^{\varnothing}\phi_i + \int_{\Omega_i} \phi_i \boldsymbol{f}^{\varnothing}(u_h)\boldsymbol{\cdot}\,\boldsymbol{\nabla}^{\varnothing} R - \int_{\partial\Omega_i^{\partial}} R\phi_i \boldsymbol{f}^{\varnothing}(u_h)\boldsymbol{\cdot}\,\boldsymbol{n}_i^{\varnothing},$$

where $\mathcal{N}_i$ is the set of shape functions ϕ_k whose support Ω_k overlap Ω_i of ϕ_i and where

$$M_{ik}^{\varnothing} \stackrel{\text{def}}{=} \int_{\Omega_{ik}} R\phi_i\phi_k,$$

with $\Omega_{ik} = \Omega_i \cap \Omega_k$. By resorting to the so-called flux reinterpolation technique,[7] the flux function $\boldsymbol{f}^{\varnothing}(u_h)$ is now expanded using the same shape functions $\phi_h \in V_h$ as follows

$$\boldsymbol{f}^{\varnothing}\big(u_h(Z,R,\theta,t)\big) \simeq \sum_{k\in\mathcal{N}} \boldsymbol{f}_k^{\varnothing}(t)\phi_k(Z,R,\theta),$$

where $\boldsymbol{f}_k^{\varnothing}(t) = \boldsymbol{f}^{\varnothing}(u_k(t))$, to obtain

$$\begin{aligned}\sum_{k\in\mathcal{N}_i} M_{ik}^{\varnothing}\frac{\mathrm{d}u_k}{\mathrm{d}t} = \sum_{k\in\mathcal{N}_i} \boldsymbol{f}_k^{\varnothing}(t)\cdot\int_{\Omega_{ik}} R\phi_k\boldsymbol{\nabla}^{\varnothing}\phi_i + \sum_{k\in\mathcal{N}_i} \boldsymbol{f}_k^{\varnothing}(t)\cdot\int_{\Omega_{ik}} \phi_i\phi_k\boldsymbol{\nabla}^{\varnothing}R \\ - \sum_{k\in\mathcal{N}_i^{\partial}} \boldsymbol{f}_k^{\varnothing}(t)\cdot\int_{\partial\Omega_{ik}^{\partial}} R\phi_i\phi_k\boldsymbol{n}_i^{\varnothing},\end{aligned}$$

where $\partial\Omega_{ik}^{\partial} = \partial\Omega_i \cap \partial\Omega_k \cap \partial\Omega$, and $\mathcal{N}_i^{\partial}$ is the set of all boundary nodes of Ω_i. The above spatially discrete form of the scalar equation (2) simplifies to[6]

$$\begin{aligned}\sum_{k\in N_i} M_{ik}^{\varnothing}\frac{\mathrm{d}u_k}{\mathrm{d}t} = -\sum_{k\in N_i,\neq}\left(\frac{\boldsymbol{f}_k^{\varnothing}+\boldsymbol{f}_i^{\varnothing}}{2}\cdot\boldsymbol{\eta}_{ik}^{\varnothing} - \frac{\boldsymbol{f}_k^{\varnothing}-\boldsymbol{f}_i^{\varnothing}}{2}\cdot\boldsymbol{\zeta}_{ik}^{\varnothing}\right) \\ + \boldsymbol{f}_i^{\varnothing}\cdot\widehat{\boldsymbol{L}}_i^{\varnothing} - \sum_{k\in\mathcal{N}_{i,\neq}^{\partial}}\frac{\boldsymbol{f}_k^{\varnothing}-\boldsymbol{f}_i^{\varnothing}}{2}\cdot\boldsymbol{\chi}_{ik}^{\varnothing} - \boldsymbol{f}_i^{\varnothing}\cdot\boldsymbol{\xi}_i^{\varnothing},\end{aligned} \tag{5}$$

where $\mathcal{N}_{i,\neq} = \mathcal{N}_i\backslash\{i\}$ and $\mathcal{N}_{i,\neq}^{\partial} = \mathcal{N}_i^{\partial}\backslash\{i\}$. In the expression above, the following FE metric quantities,

$$M_{ik}^{\varnothing} \stackrel{\text{def}}{=} \int_{\Omega_{ik}} R\phi_i\phi_k, \qquad M_{ik} \stackrel{\text{def}}{=} \int_{\Omega_{ik}} \phi_i\phi_k, \qquad \boldsymbol{\zeta}_{ik}^{\varnothing} \stackrel{\text{def}}{=} \int_{\Omega_{ik}} \phi_i\phi_k\hat{\boldsymbol{R}}, \qquad \widehat{\boldsymbol{L}}_i^{\varnothing} \stackrel{\text{def}}{=} \sum_{k\in\mathcal{N}_i}\boldsymbol{\zeta}_{ik}^{\varnothing} = \int_{\Omega_{ik}}\phi_i\hat{\boldsymbol{R}},$$
$$\boldsymbol{\eta}_{ik}^{\varnothing} \stackrel{\text{def}}{=} \int_{\Omega_{ik}} R(\phi_i\boldsymbol{\nabla}^{\varnothing}\phi_k - \phi_k\boldsymbol{\nabla}^{\varnothing}\phi_i), \qquad \boldsymbol{\chi}_{ik}^{\varnothing} \stackrel{\text{def}}{=} \int_{\partial\Omega_{ik}^{\partial}} R\phi_i\phi_k, \qquad \boldsymbol{\xi}_i^{\varnothing} \stackrel{\text{def}}{=} \int_{\partial\Omega_{ik}^{\partial}} R\phi_i.$$

have been introduced. In the next section, the corresponding FV metrics are derived.

2.2 Edge-based finite volume discretization

The spatially discrete form of the scalar conservation law (2) is now obtained according to the node-centred finite volume approach.[8] To this purpose, the integral form of (2)

times the radial coordinate R is enforced over a finite number of non-overlapping finite volumes $\mathcal{C}_i$, with boundary $\partial\mathcal{C}_i$, to obtain,

$$\frac{\mathrm{d}}{\mathrm{d}t}\int_{\mathcal{C}_i} Ru = -\oint_{\partial\mathcal{C}_i} R\boldsymbol{\nabla}^{\varnothing}\cdot\boldsymbol{f}^{\varnothing}, \quad \forall\mathcal{C}_i\subseteq\Omega.$$

By integrating by parts the right hand side and by applying the Gauss theorem the equation above reads

$$\frac{\mathrm{d}}{\mathrm{d}t}\int_{\mathcal{C}_i} Ru = -\oint_{\partial\mathcal{C}_i} R\boldsymbol{f}^{\varnothing}\cdot\boldsymbol{n}_i^{\varnothing} + \int_{\mathcal{C}_i}\boldsymbol{f}^{\varnothing}\cdot\hat{\boldsymbol{R}}, \quad \forall i\in\mathcal{N}.$$

where $\boldsymbol{n}_i^{\varnothing}$ is the outward normal to $\mathcal{C}_i\subseteq\Omega$. Note that each finite volume $\mathcal{C}_i$ surrounds one and only one node of the triangulation. Over each control volume $\mathcal{C}_i$ the cell-averaged unknown is introduced as follows

$$u(Z,R,\theta,t)\simeq u_i(t)=\frac{1}{V_i}\int_{\mathcal{C}_i} u(Z,R,\theta,t),$$

where V_i is the volume of the i-th cell. Therefore

$$V_i^{\varnothing}\frac{\mathrm{d}u_i}{\mathrm{d}t} = -\oint_{\partial\mathcal{C}_i} R\boldsymbol{f}^{\varnothing}\cdot\boldsymbol{n}_i^{\varnothing} + \int_{\mathcal{C}_i}\boldsymbol{f}^{\varnothing}\cdot\hat{\boldsymbol{R}}, \qquad \text{where} \quad V_i^{\varnothing}\overset{\text{def}}{=}\int_{\mathcal{C}_i} R \tag{6}$$

The boundary integral on the right hand side is now split into interface or edge contributions as follows

$$V_i^{\varnothing}\frac{\mathrm{d}u_i}{\mathrm{d}t} = -\sum_{k\in\mathcal{N}_{i,\neq}}\int_{\partial\mathcal{C}_{ik}} R\boldsymbol{f}^{\varnothing}\cdot\boldsymbol{n}_i^{\varnothing} - \int_{\partial\mathcal{C}_i^{\partial}} R\boldsymbol{f}^{\varnothing}\cdot\boldsymbol{n}_i^{\varnothing} + \int_{\mathcal{C}_i}\boldsymbol{f}^{\varnothing}\cdot\hat{\boldsymbol{R}}, \tag{7}$$

where $\mathcal{N}_{i,\neq}$ is the set of the finite volume $\mathcal{C}_k$ sharing a boundary with $\mathcal{C}_i$, excluding $\mathcal{C}_i$ and where $\partial\mathcal{C}_{ik}=\partial\mathcal{C}_i\cap\partial\mathcal{C}_k\neq\emptyset, k\neq i$, is the so-called cell interface. As it is standard practice, the flux vector is assumed to be constant over each cell interface. Under this assumption, the domain and boundary contributions read

$$\int_{\partial\mathcal{C}_{ik}} R\boldsymbol{f}^{\varnothing}\cdot\boldsymbol{n}_i^{\varnothing}\simeq\boldsymbol{f}_{ik}^{\varnothing}\cdot\int_{\partial\mathcal{C}_{ik}} R\boldsymbol{n}_i^{\varnothing}=\boldsymbol{f}_{ik}^{\varnothing}\cdot\boldsymbol{\nu}_{ik}^{\varnothing} \qquad \text{with} \qquad \boldsymbol{\nu}_{ik}^{\varnothing}\overset{\text{def}}{=}\int_{\partial\mathcal{C}_{ik}} R\boldsymbol{n}_i^{\varnothing} \qquad \text{and}$$
$$\int_{\partial\mathcal{C}_i^{\partial}} R\boldsymbol{f}^{\varnothing}\cdot\boldsymbol{n}_i^{\varnothing}\simeq\boldsymbol{f}_i^{\varnothing}\cdot\int_{\partial\mathcal{C}_i^{\partial}} R\boldsymbol{n}_i^{\varnothing}=\boldsymbol{f}_i^{\varnothing}\cdot\boldsymbol{\nu}_i^{\varnothing} \qquad \text{with} \qquad \boldsymbol{\nu}_i^{\varnothing}\overset{\text{def}}{=}\int_{\partial\mathcal{C}_i^{\partial}} R\boldsymbol{n}_i^{\varnothing},$$

respectively. If a second-order centred approximation of the fluxes is considered, namely, $\boldsymbol{f}_{ik}=(\boldsymbol{f}_i^{\varnothing}+\boldsymbol{f}_k^{\varnothing})/2$, the final form of the finite volume approximation of (2) reads,

$$V_i^{\varnothing}\frac{\mathrm{d}u_i}{\mathrm{d}t} = -\sum_{k\in\mathcal{N}_{i,\neq}}\frac{\boldsymbol{f}_i^{\varnothing}+\boldsymbol{f}_k^{\varnothing}}{2}\cdot\boldsymbol{\nu}_{ik}^{\varnothing}+\boldsymbol{f}_i^{\varnothing}\cdot\widehat{\boldsymbol{V}}_i^{\varnothing}-\boldsymbol{f}_i^{\varnothing}\cdot\boldsymbol{\nu}_i^{\varnothing} \quad \text{with } \widehat{\boldsymbol{V}}_i^{\varnothing}\overset{\text{def}}{=}\int_{\mathcal{C}_i}\hat{\boldsymbol{R}}, \tag{8}$$

to be compared with the corresponding FE discretization (5).

2.3 Finite Element/Volume equivalence

The equivalence conditions relating the above FV metric quantities and the FE ones defined in the previous section are now derived. To this purpose, relevant properties of the FE and FV discretizations are briefly recalled.

Considering FE metric quantities first, from its definition the vector $\boldsymbol{\eta}_{ik}^{\varnothing}$ is asymmetric, namely,

$$\boldsymbol{\eta}_{ik}^{\varnothing} = -\boldsymbol{\eta}_{ki}^{\varnothing}, \tag{9}$$

which will be referred in the following as property FEM-a. Property FEM-b is obtained by noting that

$$\sum_{k \in \mathcal{N}_i} (\boldsymbol{\eta}_{ik}^{\varnothing} - \boldsymbol{\zeta}_{ik}^{\varnothing}) + \boldsymbol{\xi}_i^{\varnothing} = \mathbf{0},$$

which gives immediately

$$\widehat{\boldsymbol{L}}_i^{\varnothing} = \sum_{k \in \mathcal{N}_{i,\neq}} \boldsymbol{\eta}_{ik}^{\varnothing} + \boldsymbol{\xi}_i^{\varnothing}. \tag{10}$$

Property FEM-c stems from the following identity

$$\int_{\Omega_i} R\phi_i \boldsymbol{\nabla}^{\varnothing} \cdot \boldsymbol{p}^{\varnothing} = \int_{\Omega_i} 3R\phi_i = 3L_i^{\varnothing} = 3 \sum_{k \in N_i} M_{ik}^{\varnothing},$$

where $\boldsymbol{p}^{\varnothing}$ is the position vector, $\boldsymbol{p}^{\varnothing} = Z\hat{\boldsymbol{Z}} + R\hat{\boldsymbol{R}}(\theta)$. On the other hand, by integrating by parts, one also has

$$\int_{\Omega_i} R\phi_i \boldsymbol{\nabla}^{\varnothing} \cdot \boldsymbol{p}^{\varnothing} = \int_{\partial\Omega_i^{\partial}} R\phi_i \boldsymbol{p}^{\varnothing} \cdot \boldsymbol{n}_i^{\varnothing} - \int_{\Omega_i} \phi_i \boldsymbol{p}^{\varnothing} \cdot \hat{\boldsymbol{R}} - \int_{\Omega_i} R\boldsymbol{p}^{\varnothing} \cdot \boldsymbol{\nabla}^{\varnothing} \phi_i. \tag{11}$$

By substituting the exact expansion $\boldsymbol{p}^{\varnothing} = \sum_{k \in \mathcal{N}_i} \boldsymbol{p}_k^{\varnothing} \phi_k$, Eq. (11) reads

$$3L_i^{\varnothing} = + \sum_{k \in \mathcal{N}_i^{\partial}} \boldsymbol{p}_k^{\varnothing} \cdot \int_{\partial\Omega_{ik}^{\partial}} R\phi_i \phi_k \boldsymbol{n}_i^{\varnothing} - \sum_{k \in \mathcal{N}_i} \boldsymbol{p}_k^{\varnothing} \cdot \int_{\Omega_{ik}} \phi_i \phi_k \hat{\boldsymbol{R}} - \sum_{k \in \mathcal{N}_i} \boldsymbol{p}_k^{\varnothing} \cdot \int_{\Omega_{ik}} R\phi_k \boldsymbol{\nabla}^{\varnothing} \phi_i,$$

which, from the node-pair representation described in section 2.1, can be written as

$$\begin{aligned} 3L_i^{\varnothing} = \sum_{k \in \mathcal{N}_{i,\neq}} & \left[\frac{\boldsymbol{p}_k^{\varnothing} + \boldsymbol{p}_i^{\varnothing}}{2} \cdot \boldsymbol{\eta}_{ik}^{\varnothing} - \frac{\boldsymbol{p}_k^{\varnothing} - \boldsymbol{p}_i^{\varnothing}}{2} \cdot \boldsymbol{\zeta}_{ik}^{\varnothing} \right] \\ & - \widehat{\boldsymbol{L}}_i^{\varnothing} \cdot \boldsymbol{p}_i^{\varnothing} + \sum_{k \in \mathcal{N}_{i,\neq}^{\partial}} \frac{\boldsymbol{p}_k^{\varnothing} - \boldsymbol{p}_i^{\varnothing}}{2} \cdot \boldsymbol{\chi}_{ik}^{\varnothing} + \boldsymbol{p}_i^{\varnothing} \cdot \boldsymbol{\xi}_i^{\varnothing}. \end{aligned}$$

By substituting property FEM-b in the above identity, one finally obtain property FEM-c as

$$3L_i^{\varnothing} = \sum_{k \in \mathcal{N}_{i,\neq}} \left[\frac{\boldsymbol{p}_k^{\varnothing} + \boldsymbol{p}_i^{\varnothing}}{2} \cdot \boldsymbol{\eta}_{ik}^{\varnothing} - \frac{\boldsymbol{p}_k^{\varnothing} - \boldsymbol{p}_i^{\varnothing}}{2} \cdot \boldsymbol{\zeta}_{ik}^{\varnothing} \right] + \sum_{k \in \mathcal{N}_{i,\neq}^{\partial}} \frac{\boldsymbol{p}_k^{\varnothing} - \boldsymbol{p}_i^{\varnothing}}{2} \cdot \boldsymbol{\chi}_{ik}^{\varnothing}. \tag{12}$$

Considering now FV metric quantities, from the fact that $\boldsymbol{n}_i^{\varnothing} = -\boldsymbol{n}_k^{\varnothing}$ over $\partial\mathcal{C}_{ik}$, property FVM-a reads

$$\boldsymbol{\nu}_{ik}^{\varnothing} = -\boldsymbol{\nu}_{ki}^{\varnothing}, \tag{13}$$

which corresponds to the conservation property of the scheme. From the Gauss theorem, one also has

$$\int_{\mathcal{C}_i} \boldsymbol{\nabla}^{\varnothing} R = \oint_{\partial\mathcal{C}_i} R\boldsymbol{n}_i^{\varnothing},$$

which, from the definition of FV metric quantities, gives property FVM-b as

$$\widehat{\boldsymbol{V}}_i^{\varnothing} = \sum_{k\in\mathcal{N}_{i,\neq}} \boldsymbol{\nu}_{ik}^{\varnothing} + \boldsymbol{\nu}_i^{\varnothing}. \tag{14}$$

Property FVM-c is obtained by noting that

$$3V_i^{\varnothing} = \int_{\mathcal{C}_i} R\boldsymbol{\nabla}^{\varnothing} \cdot \boldsymbol{p}^{\varnothing} = \oint_{\partial\mathcal{C}_i} R\boldsymbol{p}^{\varnothing} \cdot \boldsymbol{n}_i^{\varnothing} - \int_{\mathcal{C}_i} \hat{\boldsymbol{R}} \cdot \boldsymbol{p}^{\varnothing}. \tag{15}$$

The right hand side of (15) is now computed by means of the FV discretization described in section 2.2 as

$$3V_i^{\varnothing} = \sum_{k\in\mathcal{N}_{i,\neq}} \frac{\boldsymbol{p}_k^{\varnothing} + \boldsymbol{p}_i^{\varnothing}}{2} \cdot \boldsymbol{\nu}_{ik}^{\varnothing} - \boldsymbol{p}_i^{\varnothing} \cdot \widehat{\boldsymbol{L}}_i^{\varnothing} + \boldsymbol{p}_i^{\varnothing} \cdot \boldsymbol{\nu}_i^{\varnothing},$$

which from property FVM-b becomes

$$3V_i^{\varnothing} = \sum_{k\in\mathcal{N}_{i,\neq}} \frac{\boldsymbol{p}_k^{\varnothing} + \boldsymbol{p}_i^{\varnothing}}{2} \cdot \boldsymbol{\nu}_{ik}^{\varnothing}. \tag{16}$$

Therefore, a FV approximation can be formally obtained from FE metric quantities defined over the same grid points by setting (see properties FEM/FVM-a and -b)

$$\boldsymbol{\nu}_{ik}^{\varnothing} = \boldsymbol{\eta}_{ik}^{\varnothing}, \quad \boldsymbol{\nu}_i^{\varnothing} = \boldsymbol{\xi}_i^{\varnothing}, \quad \widehat{\boldsymbol{V}}_i^{\varnothing} = \widehat{\boldsymbol{L}}_i^{\varnothing}.$$

Note that the mass lumping approximation,

$$\sum_{k\in N_i} M_{ik}^{\varnothing} \frac{\mathrm{d}u_k}{\mathrm{d}t} \simeq L_i^{\varnothing} \frac{\mathrm{d}u_i}{\mathrm{d}t}$$

is to be introduced in (5) for the equivalence conditions to be applicable. By subtracting (12) to (16), one finally has

$$V_i^{\varnothing} = L_i^{\varnothing} + \sum_{k\in\mathcal{N}_{i,\neq}} \frac{\boldsymbol{p}_k^{\varnothing} - \boldsymbol{p}_i^{\varnothing}}{6} \cdot \boldsymbol{\zeta}_{ik}^{\varnothing} - \sum_{k\in\mathcal{N}_{i,\neq}^{\partial}} \frac{\boldsymbol{p}_k^{\varnothing} - \boldsymbol{p}_i^{\varnothing}}{6} \cdot \boldsymbol{\chi}_{ik}^{\varnothing}. \tag{17}$$

It is remarkable that, differently from the Cartesian case,[3,4] in the cylindrical reference the FV cell is not coincident with the FE lumped mass matrix. Moreover, the shape of the FV cells that guarantees equivalence with FE discretization still remains to be determined.

2.4 Fully discrete form of the Euler equations in cylindrical coordinates

The Euler equations for compressible inviscid flows of interest here are now briefly recalled. The differential form reads,

$$\frac{\partial \mathbf{u}^{\varnothing}}{\partial t} + \boldsymbol{\nabla}^{\varnothing} \cdot \mathbf{f}^{\varnothing} = \frac{1}{R} \boldsymbol{s}^{\varnothing}, \tag{18}$$

where $\mathbf{u}^{\varnothing}$, $\mathbf{u}^{\varnothing}(Z, R, \theta, t) = (\rho, \boldsymbol{m}^{\varnothing}, E^{\mathrm{t}})^{\mathrm{T}}$, with ρ density, $\boldsymbol{m}^{\varnothing} = (m_Z, m_R, m_\theta)^{\mathrm{T}}$ momentum and E^{t} total energy per unit mass, and where

$$\mathbf{f}^{\varnothing} = \begin{pmatrix} m_Z & m_R & m_\theta \\ \dfrac{m_Z^2}{\rho} + \Pi & \dfrac{m_R m_Z}{\rho} & \dfrac{m_\theta m_Z}{\rho} \\ \dfrac{m_Z m_R}{\rho} & \dfrac{m_R^2}{\rho} + \Pi & \dfrac{m_\theta m_R}{\rho} \\ \dfrac{m_Z m_\theta}{\rho} & \dfrac{m_R m_\theta}{\rho} & \dfrac{m_\theta^2}{\rho} + \Pi \\ \dfrac{m_Z}{\rho}\left(E^t + \Pi\right) & \dfrac{m_R}{\rho}\left(E^t + \Pi\right) & \dfrac{m_\theta}{\rho}\left(E^t + \Pi\right) \end{pmatrix} \quad \text{and} \quad \boldsymbol{s}^{\varnothing} = \begin{pmatrix} 0 \\ 0 \\ \dfrac{m_\theta^2}{\rho} + \Pi \\ \dfrac{m_\theta m_R}{\rho} \\ 0 \end{pmatrix},$$

are the matrix of the fluxes and the source term, respectively. The FV spatially-discrete form of the Euler equations reads

$$V_i^{\varnothing} \frac{\mathrm{d}\mathbf{u}_i^{\varnothing}}{\mathrm{d}t} = - \sum_{k \in \mathcal{N}_i, \neq} \frac{\mathbf{f}_k^{\varnothing} + \mathbf{f}_i^{\varnothing}}{2} \cdot \boldsymbol{\eta}_{ik}^{\varnothing} + L_i \boldsymbol{s}_i^{\varnothing} - \mathbf{f}_i^{\varnothing} \cdot \boldsymbol{\xi}_i^{\varnothing}, \tag{19}$$

where $\boldsymbol{s}_i^{\varnothing}(t) \stackrel{\text{def}}{=} \boldsymbol{s}^{\varnothing}(\mathbf{u}_i^{\varnothing})$ and where $V_i^{\varnothing}$ is computed from the equivalence condition (17). In the computation, a TVD[9] numerical flux is used, with the van Leer limiter.[10] The fully discrete form of the Euler system is obtained by a two-step Backward Differencing Formulæ. At each time level, a dual time-stepping technique is used to solve the time-implicit problem.[11]

3 NUMERICAL RESULTS

In the present section, numerical results for converging and diverging cylindrical and spherical shock waves are presented in the two- (Z-R and R-θ planes) and one-dimensional cases.

The case of the explosion problem[1] is considered first. The computational domain is shown in figure 1, where a representative computational grid is also shown. Initial conditions for the explosion problem are as follows. The velocity is assumed to be zero everywhere; the density is uniform and equal to 1, whereas the pressure is uniform and equal to 10 in circular region centred at the origin with radius $R = 0.5$. In the remaining

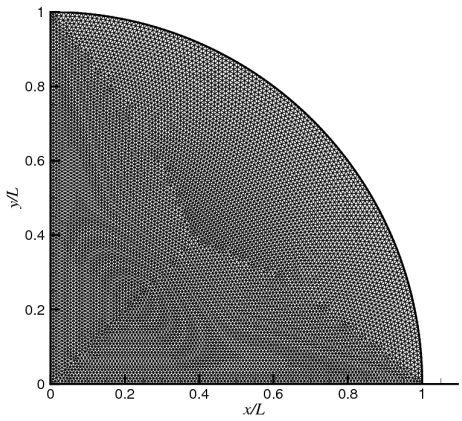

Figure 1: Exemplary grid for the explosion and implosion problems. The grid is the coarse grid made of 9 551 nodes and 18 745 triangles. The resolution along the radial direction is approximatively 0.01.

portion of the domain, the pressure is uniform and equal to 1. In all computations, the ideal gas model for nitrogen ($\gamma = c_P/c_v = 1.39$) is used. Pressure and density are made dimensionless by the corresponding value at rest (outer region), which are indicated in the following as P_{ref} and ρ_{ref}, respectively. The time is made dimensionless by $L_{\text{ref}}\sqrt{\rho_{\text{ref}}/P_{\text{ref}}}$, with L_{ref} unit length.

Numerical results are shown in figure 2, where density isolines at different time levels are shown. On the left column of figure 2, the independent variables are R and θ, namely, a cylindrical shock wave is considered. On the left hand side, a spherical problem is solved in the Z-R plane, where axial symmetry is assumed. The grid is the fine grid with 39 153 nodes 77 587 triangles and the time step is 2.5×10^{-4} for the cylindrical case and 1.5×10^{-4} for the spherical one. In both situations, a cylindrical/spherical shock wave propagates towards the outer boundary of the computational domain; the shock wave is followed by a contact discontinuity. A rarefaction wave propagates towards the origin and is then reflected outward. Note that the initial corrugation of the shock front, due to the un-even shape of the initial discontinuity caused by its discrete representation over an unstructured grid of triangles, is clearly visible also at later times. The pressure profile in figure 3 confirm the above description of the flow field and are compared against reference one-dimensional results for three different time levels. One-dimensional computations were performed over a evenly-spaced grid made of 2 001 nodes, which corresponds to an element spacing of 5×10^{-4}.

A grid dependence study is shown in figure 4. Pressure signals along the $y = 0$ axis are compared at time $t = 0.16$ for three different grid resolutions: the coarse grid is made of 9 551 nodes and 18 745 triangles, the medium one is made of 20 683 nodes and 40 841 triangles, the fine one is made of 39 153 nodes 77 587 triangles. Numerical results are find to be almost independent from the grid resolution; in the following, the fine grid is used

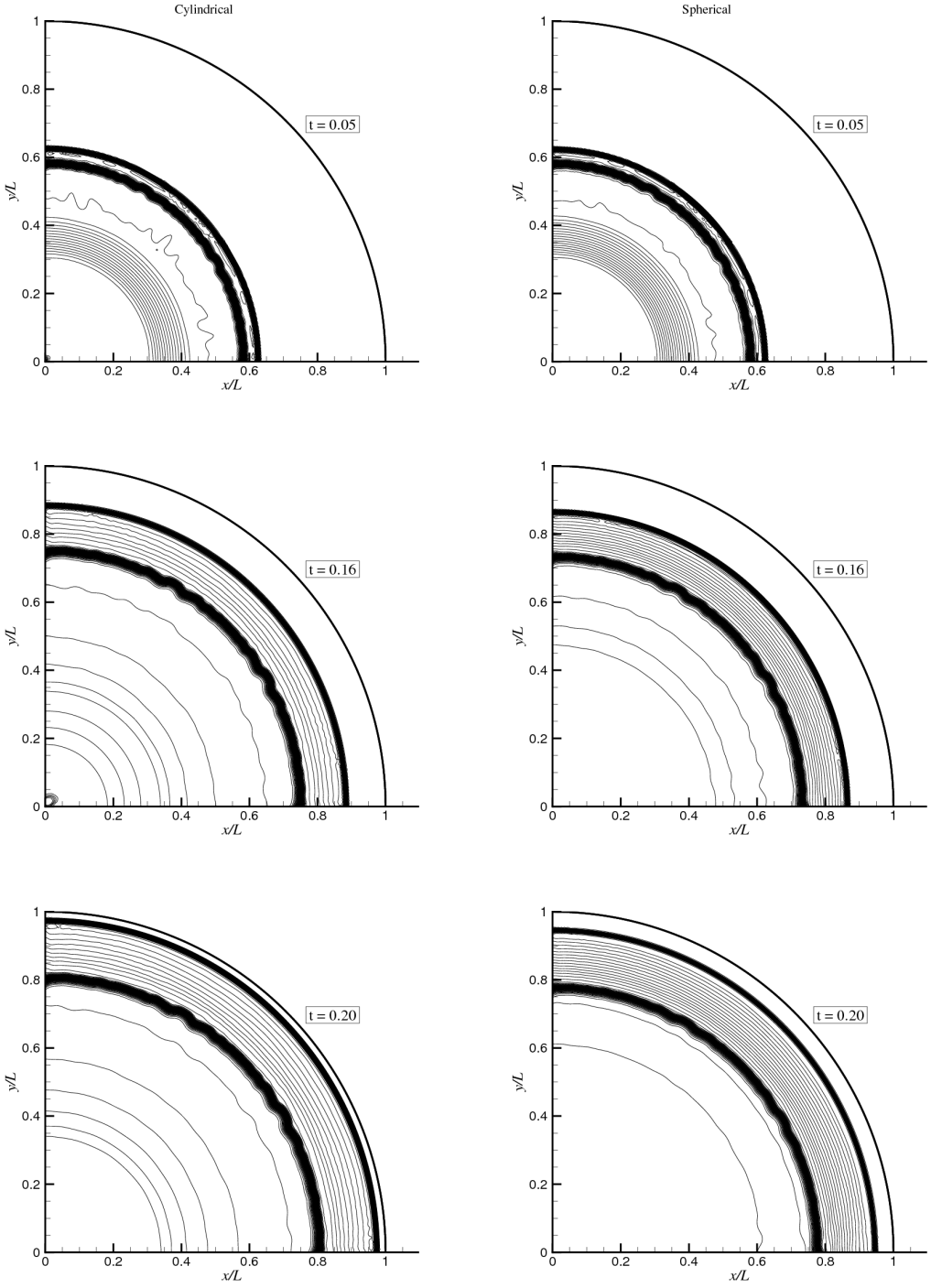

Figure 2: Density isolines for the explosion problem. Each isoline corresponds to a density difference of $\Delta\rho/\rho_{\text{ref}} = 0.03$. Left row: cylindrical problem, right row: spherical problem. Time increases from top to bottom.

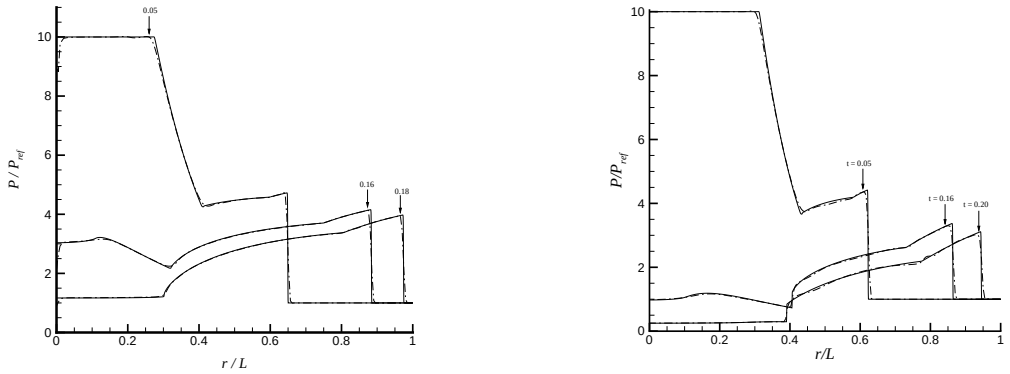

Figure 3: Pressure along the $y = 0$ axis for the explosion problem at times $t = 0.05$, $t = 0.16$ and $t = 0.20$. The solid line is the 1D reference solution, the dash-dot line is the 2D solution. Left: cylindrical problem, right: spherical problem.

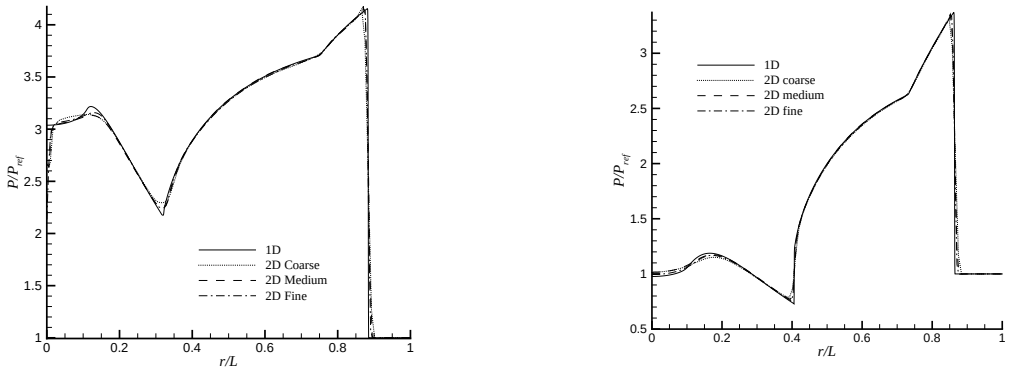

Figure 4: Comparison of pressure signals along the $y = 0$ axis for the explosion problem at time $t = 0.16$ for different grid resolutions against one dimensional simulations. Left: cylindrical case, right: spherical case.

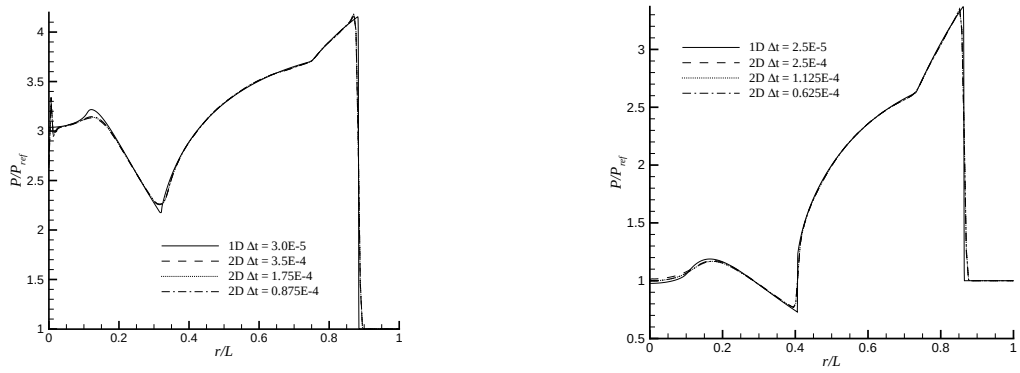

Figure 5: Comparison of pressure signals along the $y = 0$ axis for the explosion problem at time $t = 0.16$ for diverse time steps against one dimensional simulations. Left: cylindrical case, right: spherical case.

in all computations. Time step dependence can be appreciated from figure 5, where the pressure signals for three different time steps is shown at time $t = 0.16$ for the medium grid. Numerical results are found to be independent from the chosen time step. In all computations in the R-θ plane, the solution at the grid node located at the origin of the reference system suffers from a significant undershoot, which however does not propagate inside the domain and does not affect the correct propagation of the reflected waves.

In figure 6, numerical results for the so-called implosion problem[1] are shown for both the cylindrical and spherical case. The initial condition is as in the explosion problem, where now the high pressure region is the outer one and the low pressure region is at $R \leq 0.5$. The grid is the fine grid and the time step is 2.5×10^{-4} for the cylindrical (R-θ) case and 1.5×10^{-4} for the spherical (Z-R) one. A rarefaction wave propagates towards the outer boundary; a shock wave and a contact surface propagates inwards. The intensity of the shock increases as it moves towards the origin; when the shock wave is reflected at the origin, a region of high pressure/temperature is observed. In the spherical case, this effect is more evident.

Converging shock waves are used in experimental facility to attain high pressure and high temperature state to be used e.g. in Inertial Confinement Fusion (ICF) or sonoluminescence studies. A major drawback of this kind of technique is the occurrence of shock front instabilities in converging cylindrical and spherical shock waves.[5] Recently, the inclusion of obstacles in the flow field has been proposed as a mean to transform a converging cylindrical shock into a polygonal one,[12–14] which does not suffer from the aforementioned front instabilities. An example is given in figure 7, where four cylindrical obstacles are used to transform the converging cylindrical shock wave into a square-shaped shock wave. The computational domain is made discrete by an unstructured grid made of 36 713 nodes and 72 612 triangle. In all computations with obstacles, the Courant-Friedrichs-Lewy number is 0.5. The symmetry of the problem is not enforced to reduce

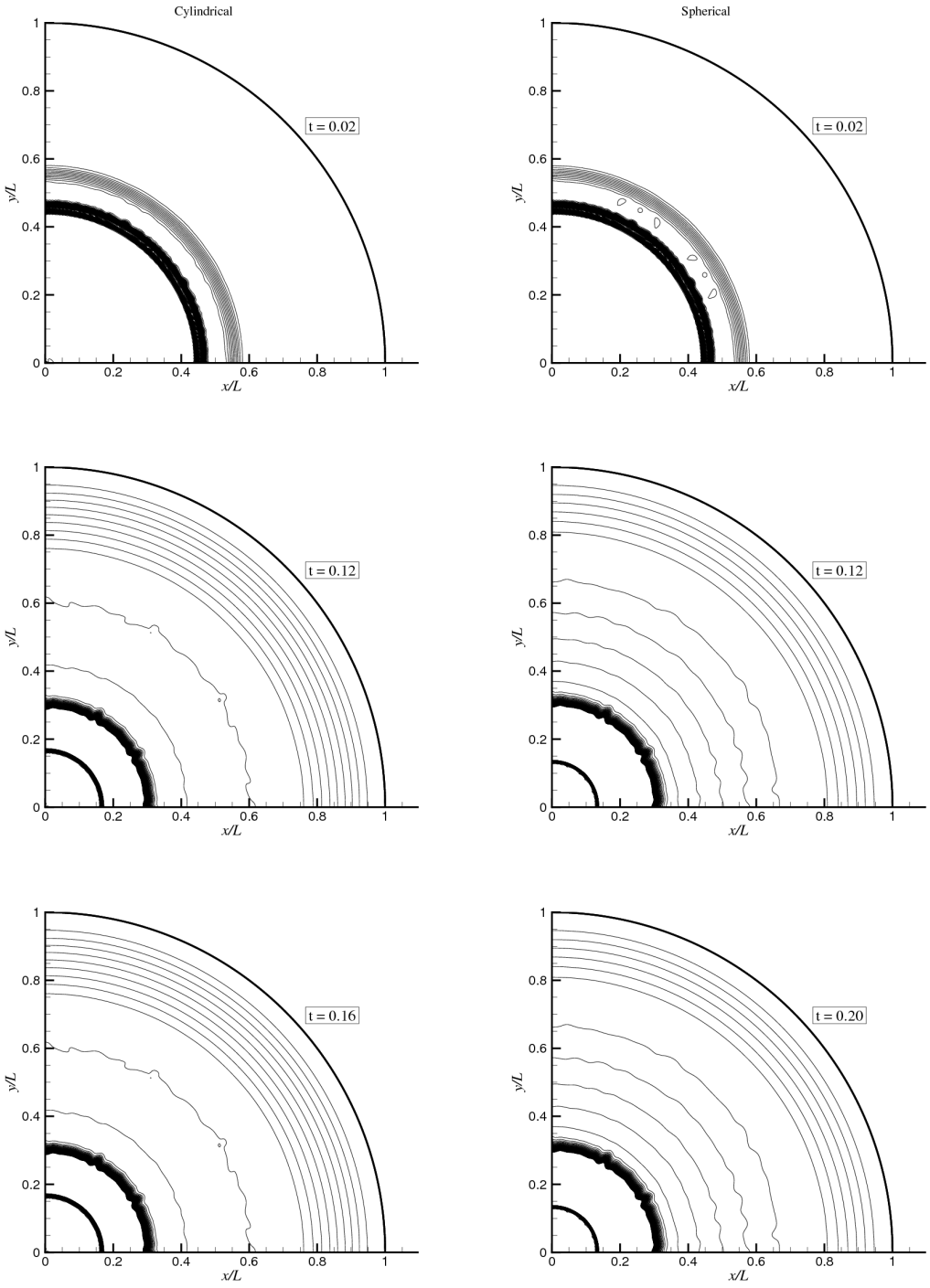

Figure 6: Density isolines for the implosion problem. Each isoline corresponds to a density difference of $\Delta\rho/\rho_{\text{ref}} = 0.03$. Left row: cylindrical problem, right row: spherical problem. Time increases from top to bottom.

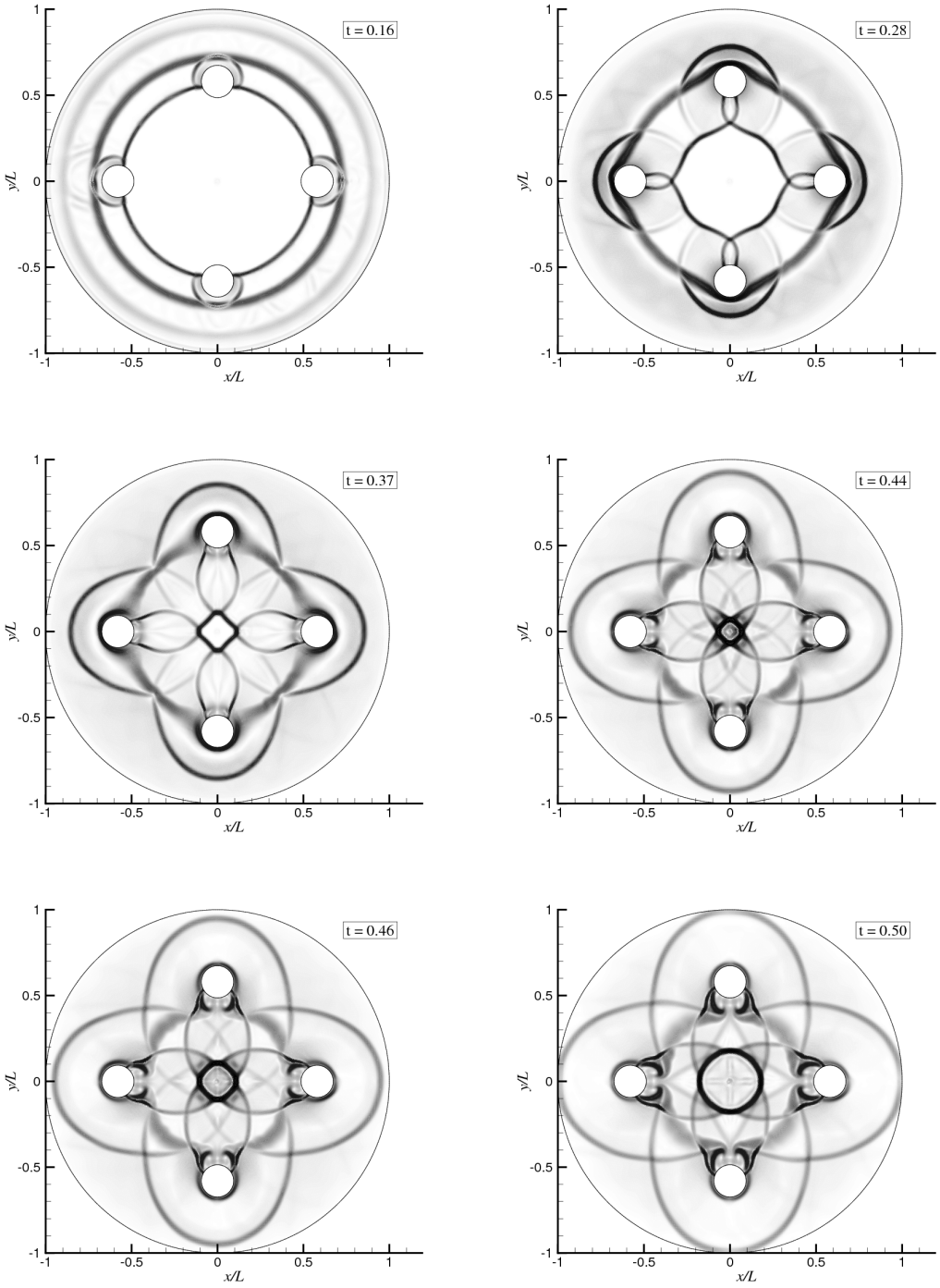

Figure 7: Numerical Schlieren of the cylindrical implosion problem with four cylindrical obstacles. Time increases from left to right and from top to bottom. The first three plots show the converging shock wave before reflection at the origin.

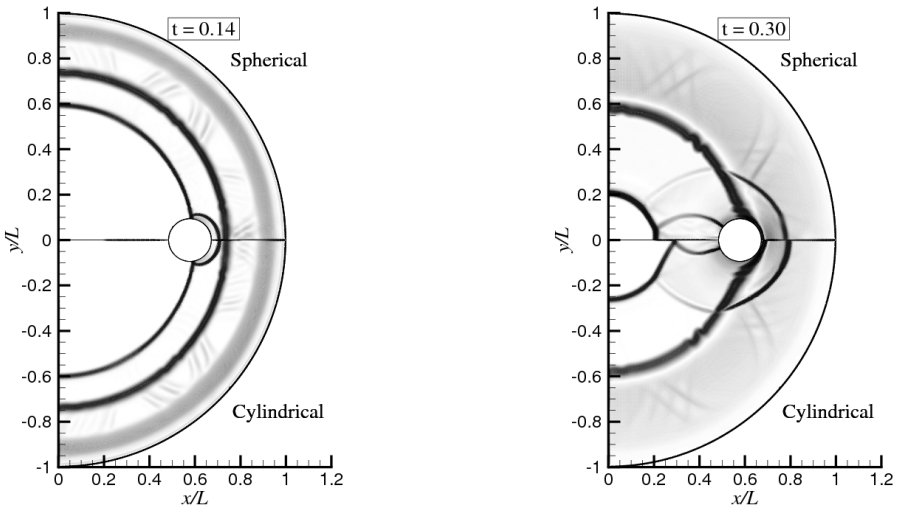

Figure 8: Numerical Schlieren of the implosion problem with two obstacles (only one is shown because of symmetry). Left: before shock-obstacle interaction. Right: after shock-obstacle interaction. In each plot, the upper half shows the spherical problem, the lower half the cylindrical one.

the computational burden to verify the capability of the scheme to reproduce correctly symmetry boundaries within the domain. The initial conditions correspond to a pressure and density discontinuity at $R = 0.875$, with a pressure and density ratio of 10 across the initial discontinuity. Numerical results are in good agreement with similar cases available in the literature, where additional details on the problem geometry can be found.[12]

In the present study, the case of a spherical converging shock wave is also considered. As mentioned above, for a given pressure/density initial ratio, a spherical shock wave results in higher pressure/temperature at the origin. Figure 8 reports on a comparison between spherical shock wave being diffracted from a spherical obstacle and a cylindrical shock wave encountering a cylindrical obstacle. In the computations, a grid made of 22 649 nodes and 44 781 triangles was used. In the cylindrical case, the interaction between the shock and the obstacle results in the formation of a planar portion of the shock wave, which for the four-obstacle case eventually results in the formation of a square-shaped shock. This is not the case for the spherical obstacle, in which the modification of the shock geometry is less relevant. This is possibly due to the limited area ratio of the obstacle frontal area and that of the propagating shock waves.[15] A geometry more similar to that considered in the cylindrical case would have been obtained by inserting a number of spherical obstacles providing the same area blockage and would have required complex three-dimensional simulations, which are left for future investigations.

4 CONCLUSIONS

A novel unstructured-grid hybrid finite element/volume method in a cylindrical reference was presented. The proposed approach represents an extension of the well-known node-pair scheme of Selmin[3] to the case of cylindrical coordinates and moves from suitable equivalence conditions linking finite element integrals to the corresponding finite volume metrics, such as the cell volume or the integrated normals. Differently from previous references, equivalence conditions were derived here without introducing any approximation and allowed to determine all needed finite volume metric quantities from finite element ones.

Numerical results are presented for two-dimensional compressible flows in the polar and axisymmetric cases. These include numerical simulation of the explosion and implosion problems, in which an initial discontinuity in pressure results in the formation of a diverging and converging shock, respectively. The computed pressure and density profile agree fairly well with one-dimensional simulation in cylindrical and spherical symmetry over a very fine grid.

The proposed approach was applied to the simulation of converging shock waves including their interaction with cylindrical obstacles, a case study that is relevant for Inertial Confinement Fusion (ICF) and sonoluminescence studies. Cylindrical obstacles are placed within the flow field to modify the cylindrical shock geometry into that of a polygonal shock wave, to increase the shock front stability. In the present study, spherical obstacles were considered to modify the geometry of a spherical converging shock waves. With respect to their cylindrical counterpart, spherical obstacles introduces a smaller modification to the shock front and are not sufficient, at least for the geometry considered here, to reshape the spherical shock wave into a polygonal one.

REFERENCES

[1] L. I. Sedov. *Similarity and dimensional methods in mechanics.* Academic Press, 1959.

[2] L. Fezou and B. Stoufflet. A class of implicit upwind schemes for Euler simulations with unstructured meshes. *J. Comput. Phys.*, 84(1):174–206, 1989.

[3] V. Selmin. The node-centred finite volume approach: bridge between finite differences and finite elements. *Comp. Meth. Appl. Mech. Engng.*, 102:107–138, 1993.

[4] V. Selmin and L. Formaggia. Unified construction of finite element and finite volume discretizations for compressible flows. *Int. J. Numer. Meth. Eng.*, 39:1–32, 1996.

[5] H. B. Chen, L. Zhang, and E. Panarella. Stability of imploding spherical shock waves. *Journal of Fusion Energy*, 14:389–392, 1995.

[6] A. Guardone and L. Vigevano. Finite element/volume solution to axisymmetric conservation laws. *J. Comput. Phys.*, 224:489–518, 2007.

[7] J. Donea and A. Huerta. *Finite element methods for flow problems*. Wiley, 2002.

[8] R. J. LeVeque. *Finite volume methods for conservation laws and hyperbolic systems*. Cambridge University Press, 2002.

[9] A. Harten and J. M. Hyman. Self adjusting grid methods for one-dimensional hyperbolic conservation laws. *J. Comput. Phys.*, 50:253–269, 1983.

[10] B. van Leer. Towards the ultimate conservative difference scheme II. Monotoniticy and conservation combined in a second order scheme. *J. Comput. Phys.*, 14:361–370, 1974.

[11] V. Venkatakrishnan and D. J. Mavriplis. Implicit method for the computation of unsteady flows on unstructured grids. *J. Comput. Phys.*, 127:380–397, 1996.

[12] V. Eliasson, N. Tillmark, A. J. Szeri, and N. Apazidis. Light emission during shock wave focusing in air and argon. *Phys. Fluids*, 19:106106, 2007.

[13] V. Eliasson, M. Kjellander, and N. Tillmark. Regular versus Mach reflection for converging polygonal shocks. *Shock Waves*, 17:43–50, 2007.

[14] V. Eliasson, N. Apazidis, and N. Tillmark. Controlling the form of strong converging shocks by means of disturbances. *Shock Waves*, 17:29–42, 2007.

[15] H. Shi and K. Yamamura. The interaction between shock waves and solid spheres arrays in a shock tube. *Acta Mech. Sinica*, 20(3):219–227, 2004.